



# Many-body suppression of optically induced inelastic scattering in a weakly interacting Fermi gas near a Fano-Feshbach resonance

Camen A. Royse, J. Huang , and J. E. Thomas \*Department of Physics, [North Carolina State University](#), Raleigh, North Carolina 27695, USA

(Received 12 June 2024; accepted 28 June 2024; published 20 August 2024)

We derive a model to explain the observed suppression of optically induced loss in a weakly interacting Fermi gas as the  $s$ -wave scattering length is increased [C. A. Royse *et al.*, [Phys. Rev. Lett.](#) **133**, 083404 (2024)]. We incorporate spin-dependent loss into a quasiclassical collective spin vector model to show that loss suppression occurs via a transition to a magnetized dynamical state, where two-body  $s$ -wave scattering is inhibited via the Pauli principle. By comparing measurements in mixtures and coherently prepared samples, we show that the data are quantitatively explained by the model, which is applicable to the optical control of energy-space lattices for new quantum simulators.

DOI: [10.1103/PhysRevA.110.023322](#)

## I. INTRODUCTION

Weakly interacting atomic Fermi gases, created by tuning a two-state Fermi gas near a collisional Fano-Feshbach resonance, provide a unique platform for exploring light-induced atom loss in a trapped quantum many-body spin system. Previously, photoassociation loss near a Fano-Feshbach resonance has been used to probe atom pairing in the strongly interacting BEC-BCS crossover regime [1]. Understanding light-induced loss is essential for developing new optical probes, for optical methods for engineering Hamiltonians [2–6], and for optical control of two-body scattering [7–11]. Recently, measurements of optically induced loss in a weakly interacting Fermi gas have revealed a crossover from high to low loss as the  $s$ -wave scattering length is increased [12]. This suppression is not explained by Pauli blocking [13–16], where individual atoms are prevented from recoiling into occupied momentum states in a Fermi sea. Instead, coherently prepared weakly interacting Fermi gases exhibit coherent many-body spin evolution [17–27] that dramatically modifies the light-induced loss [12].

In this paper, we develop a comprehensive model for collective suppression of optically induced loss in a weakly interacting  $^6\text{Li}$  Fermi gas, coherently prepared in a pseudospin state by a radio-frequency (rf) pulse. During the subsequent evolution period, the energy state  $|E\rangle$  of each atom in the weakly interacting gas does not change. However, each pseudospin state evolves as an energy-dependent superposition of the two lowest hyperfine states  $|1\rangle$ ,  $|2\rangle$ , allowing the cloud to be described as an energy-space spin lattice. By including spin-dependent loss in the energy-space spin lattice picture, we derive a quasiclassical collective spin vector model for the evolution of the many-body light induced loss. The model shows that dynamical loss suppression arises from the onset of a magnetized dynamical state, where the Pauli principle suppresses  $s$ -wave scattering. This mitigation of optically induced

loss is important for applying designer spatial control of the  $s$ -wave scattering length [28] to tailor the spin-spin couplings in energy-space spin lattices [see Eq. (11)], enabling new quantum simulators. Further, we measure optically induced loss in incoherent mixtures, providing the two-body loss constant for the model and probing the spin states of colliding atoms in the mixture.

Tunable two-body scattering with optically induced loss is accomplished using a collisional Fano-Feshbach resonance (Fig. 1). The resonance arises from hyperfine coupling between the triplet  $^3\Sigma_u$  continuum  $|k\rangle$  and a molecular vibrational state  $|g_1\rangle$  in the singlet  $^1\Sigma_g$  channel. At low temperatures, where  $s$ -wave scattering dominates, the  $s$ -wave scattering length  $a_s$  is controlled by a bias magnetic field  $B_z$ , which tunes the total Zeeman-hyperfine energy of an incoming pair of atoms in state  $|k\rangle$  near resonance with  $|g_1\rangle$ . In the weakly interacting regime, near the field  $B_0 = 527.18(2)$  G at which the scattering length vanishes for  $|1\rangle$ - $|2\rangle$  collisions, we find  $a_s = a'(B_z - B_0)$ , where the magnetic-field tuning rate  $a' = 3.14(8) a_0/\text{G}$  [24] with  $a_0$  the Bohr radius.

Inelastic loss is induced by an optical field  $\nu_1$  resonant with a transition from  $|g_1\rangle$  to an excited electronic molecular state  $|e\rangle$ , which spontaneously decays, causing loss of both atoms from the trap [8, 11, 28]. Here, the amplitude of state  $|g_1\rangle$  arises from hyperfine coupling to the incoming continuum states  $|k\rangle$  in the  $^3\Sigma_u$  channel. As the molecular transitions are far detuned from the atomic resonances, this method suppresses direct optical shifts and scattering from the atomic gas. Related level schemes have been used for optical control of  $a_s$  via a  $\nu_1$ -induced light shift of  $|g_1\rangle$  [7, 8, 10, 11].

An energy-space lattice is created in a “weakly interacting” Fermi gas, by tuning  $a_s$  to be small enough that the energy-changing collision rate  $\propto a_s^2$  is negligible during each measurement period. In the absence of optically induced loss, atoms remain fixed in their respective energy states, allowing the system to be described as a spin lattice in a “synthetic dimension” [29], where “sites” in the lattice correspond to the energy eigenstates of the trapping potential (Fig. 2). In our experiments, where the atoms are confined in a cigar-shaped

\*Contact author: [jethoma7@ncsu.edu](mailto:jethoma7@ncsu.edu)

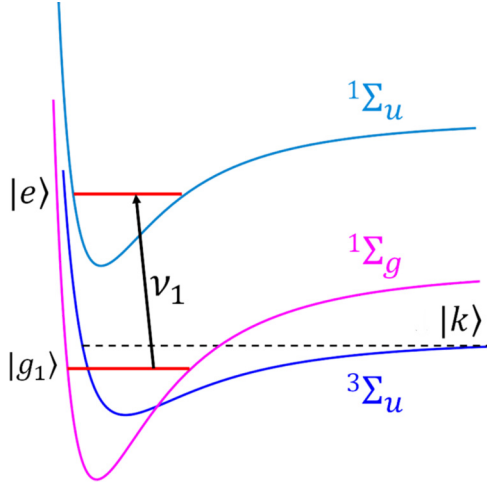


FIG. 1. Molecular states for two-body scattering near a Fano-Feshbach resonance. A pair of atoms in two different spin states collides in a relative momentum state  $|k\rangle$  in the triplet channel  $^3\Sigma_u$ , which is hyperfine coupled to a bound state  $|g_1\rangle$  in the singlet channel  $^1\Sigma_g$ . Loss is induced by an optical field  $\nu_1$  that drives a transition between  $|g_1\rangle$  and  $|e\rangle$ .

optical trap with a small axial  $x$  harmonic oscillator energy scale (compared to the Fermi energy), the axial harmonic oscillator quantum number  $0 \leq n \lesssim 650$ . Following rf excitation, each pseudospin evolves in a site  $n$ -dependent manner. A central feature of the evolution is that the overlap of the spatial probability densities  $|\phi_n(x)|^2$  and  $|\phi_{n'}(x)|^2$  enables effective long-range  $|n' - n| \gg 1$  interactions between atoms at energy sites  $n$  and  $n'$ . Spin-dependent forward scattering then produces long-range spin-spin coupling and coherent spin evolution, while optically induced inelastic scattering causes spin-dependent loss.

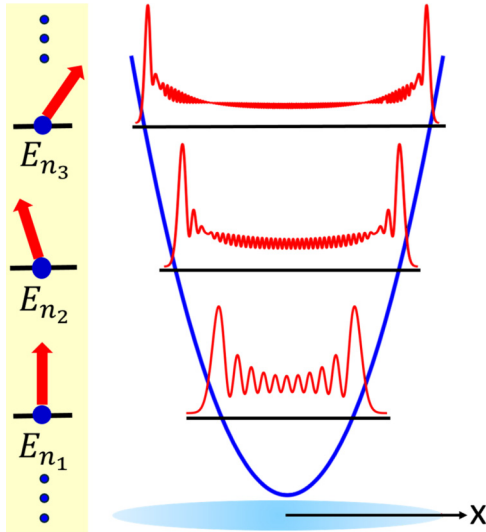


FIG. 2. Energy-space spin lattice. Atoms remain fixed at axial energy “sites”  $E_n$  in a cigar-shaped optical trap. Collective spin vectors (large arrows) for a given axial energy  $E_n$  contain pseudospins in several different transverse ( $y, z$ ) energy states. Site-to-site  $n \leftrightarrow n'$  couplings are determined by the overlap of the spatial probability distributions  $|\phi_n(x)|^2$ .

The spin dependence of the forward scattering and loss can be understood using a heuristic description. For  $s$ -wave scattering, the two-atom spatial state is symmetric under the interchange of the atom labels. The corresponding two-atom spin state must then be antisymmetric, as in Eq. (17) for the  $^3\Sigma_u$  potential. Hence, the effective scattering length and the loss rate must be proportional to a projection operator  $P_a$  for an antisymmetric two-atom spin state. For two spin-1/2 atoms,  $P_a = 1 - \mathbf{s}^2/2$ , where  $\mathbf{s} = \mathbf{s}_1 + \mathbf{s}_2$ . This gives  $P_a = 1$  for an antisymmetric spin state, where  $s = 0$  and  $P_a = 0$  for a symmetric spin state, where  $s = 1$  and  $\mathbf{s}^2 = s(s+1) = 2$ . With  $\mathbf{s}_1^2 = \mathbf{s}_2^2 = 3/4$ ,

$$P_a = \frac{1}{4} - \mathbf{s}_1 \cdot \mathbf{s}_2. \quad (1)$$

An effective spin-dependent scattering length can be described by the operator  $a_{\text{eff}} = 2a_S P_a$ , where  $2a_S$  is the  $s$ -wave scattering length for a symmetrized two-atom spatial state. For atoms in antiparallel spin states, where  $\langle \mathbf{s}_1 \cdot \mathbf{s}_2 \rangle = \langle s_{z1}s_{z2} \rangle = -1/4$ , the collision probability  $\langle P_a \rangle = 1/2$  and  $\langle a_{\text{eff}} \rangle = a_S$ , i.e., the usual scattering length. As the effective collision interaction is  $\propto P_a$ , the Heisenberg equations of motion yield  $\dot{\mathbf{s}}_1 \propto \mathbf{s}_2 \times \mathbf{s}_1$  and  $\dot{\mathbf{s}}_2 \propto \mathbf{s}_1 \times \mathbf{s}_2$ , i.e., collisions produce a rotation of each of the spins  $\mathbf{s}_1$  and  $\mathbf{s}_2$  about the conserved total spin vector  $\mathbf{s}_1 + \mathbf{s}_2$ , which is known as the identical spin rotation effect (ISRE) [22,30,31]. For atoms in parallel spin states,  $\langle \mathbf{s}_1 \times \mathbf{s}_2 \rangle = 0$ , and  $\langle \mathbf{s}_1 \cdot \mathbf{s}_2 \rangle = \langle s_{z1}s_{z2} \rangle = 1/4$ , so that the collision probability  $\langle P_a \rangle = 0$ . For parallel spins, both spin rotation and optically induced loss are suppressed.

The lattice picture simplifies the description in comparison to a real-space treatment, as the motional states of the atoms are fixed and the system evolves via pure spin dynamics, simulating a collective Heisenberg Hamiltonian [18–26]. In the following, we will use the word “site” or the phrase “energy site” to denote the “location” of an energy group in the synthetic lattice.

## II. EVOLUTION OF THE ENERGY-SPACE SPIN LATTICE WITHOUT LOSS

An rf pulse initially prepares the pseudospin state of each atom of the  $^6\text{Li}$  Fermi gas in a superposition of the two lowest hyperfine-Zeeman states, which are denoted  $|1\rangle \equiv |\uparrow_z\rangle$  and  $|2\rangle \equiv |\downarrow_z\rangle$ . In the experiments, the rf detuning is altered by the curvature of the applied bias magnetic field  $B_z \hat{\mathbf{z}}$ , which produces a spin-dependent harmonic trapping potential, due to the difference in the magnetic moments  $\mu_{\downarrow, \uparrow}$  for the two hyperfine states. For the axial (long)  $x$  direction (Fig. 2),

$$U_{\downarrow, \uparrow}(x) = -\mu_{\downarrow, \uparrow} \frac{\partial_x^2 B_z(0)}{2} x^2. \quad (2)$$

Here,  $\mu_{\downarrow, \uparrow} = -\partial E_{\downarrow, \uparrow} / \partial B$  are the magnetic-field tuning rates for the hyperfine states [24], which are nominally a Bohr magneton,  $\mu_B$ , but  $\mu_{\downarrow} - \mu_{\uparrow} \equiv \delta\mu$  is nonzero due to the differing contributions of the nuclear spin magnetic moment. For rf transitions, the harmonic oscillator state  $|n_x\rangle$  of the atom does not change. Hence, a simple first-order perturbation calculation for fixed  $n_x$  yields the shift  $\Delta_x$  of the rf detuning [32]:

$$\Delta_x = -\delta\mu \frac{\partial_x^2 B_z(0)}{2\hbar} \langle n_x | x^2 | n_x \rangle \equiv \Omega'_x E_x, \quad (3)$$

where the virial theorem gives  $\langle n_x | x^2 | n_x \rangle = E_x / (m\omega_x^2)$ .

The cigar-shaped trap (Fig. 2) is configured so that the transverse frequencies  $\omega_y$  and  $\omega_z$  are  $\simeq 30$  times larger than  $\omega_x$ . As the energy scales  $E_x$ ,  $E_y$ , and  $E_z$  for the axial and transverse directions are the same, we see that  $\langle n_y | y^2 | n_y \rangle$  and  $\langle n_z | z^2 | n_z \rangle$  are 900 times smaller than  $\langle n_x | x^2 | n_x \rangle$ . Then, cylindrical symmetry of the bias magnetic field about  $z$  and  $\nabla^2 B_z = 0$  require  $\partial_x^2 B_z(0) = \partial_y^2 B_z(0) = -\partial_z^2 B_z(0)/2$ , so that the detunings  $|\Delta_y| = |\Delta_x|/900$  and  $|\Delta_z| = |\Delta_x|/450$  are negligible. Hence, the effective rotation rate  $\Omega'_x E_x$  for the pseudospins about  $\hat{\mathbf{z}}$ , which differentiates the energy sites, depends only on the axial energy  $E_x \equiv E$ . This enables a one-dimensional (1D) approximation for the site-to-site couplings in the energy-space lattice, as we now discuss.

Site-to-site couplings, denoted by  $g(E, E')$ , arise from forward  $s$ -wave scattering between two atoms in different pseudospin states, where the ISRE [22,30,31] causes a rotation of each of the spins  $\mathbf{s}_1$  and  $\mathbf{s}_2$  about the conserved total spin vector  $\mathbf{s}_1 + \mathbf{s}_2$ , as described above. Following the discussion leading to Eq. (1), the effective spin-dependent interaction potential is given by

$$V_{12} = -\frac{4\pi\hbar^2}{m} 2a_S \delta(\mathbf{r}_1 - \mathbf{r}_2) \mathbf{s}_1 \cdot \mathbf{s}_2. \quad (4)$$

In a 1D approximation, the dependence of the site-to-site spin-spin couplings on the different transverse energy states is replaced by an average transverse probability density  $\bar{n}_\perp$  [see Eq. (11)]. Then, all pseudospins in a group with nearly the same axial energy  $E$  evolve in the same way, as described by a *collective* spin vector  $\mathbf{S}(E, t)$  for each site. We find that this 1D model, described in more detail below, is in very good agreement with our observations [24,27,33].

Without loss, the evolution of the collective spin vectors  $\mathbf{S}(E, t)$  is then described by the spin Hamiltonian  $H(E) = \boldsymbol{\omega}(E) \cdot \mathbf{S}(E)$ , where

$$\boldsymbol{\omega}(E) = \Omega'_x E \hat{\mathbf{z}} + \sum_{E' \neq E} g(E, E') \mathbf{S}(E') \quad (5)$$

with  $g(E, E') \propto a_S$  the coupling between spins at axial energy sites  $E$  and  $E' \neq E$ . In our experiments, the average coupling  $\bar{g} \simeq 1.6 \text{ Hz} \times 2\pi$  for  $a_S = 5.0 a_0$ , where  $a_0$  is the Bohr radius. The rms spread in  $\Omega'_x E$ , denoted  $\Omega'_x \sigma_E$ , is  $\simeq 1.4 \text{ Hz} \times 2\pi$ . Defining  $\mathbf{S}(E, t) = S(E, t) \hat{\mathbf{S}}(E, t)$ , where  $\hat{\mathbf{S}}(E, t)$  is a unit vector,

$$\dot{\mathbf{S}}(E) = S(E) \dot{\hat{\mathbf{S}}}(E) + \dot{S}(E) \hat{\mathbf{S}}(E). \quad (6)$$

Here  $S(E, t) = N_E(t)/2$  with  $N_E(t)$  the number of atoms with axial energy  $E$ . Neglecting loss, where  $\dot{S}(E) = 0$ , the rotation of  $\mathbf{S}(E)$ , given by the first term in Eq. (6), is determined by the Heisenberg equations:

$$\dot{\hat{\mathbf{S}}}(E, t) = \boldsymbol{\omega}(E, t) \times \hat{\mathbf{S}}(E, t). \quad (7)$$

Without loss, each  $\mathbf{S}(E, t)$  evolves via rotation, where the magnitudes  $|\mathbf{S}(E, t)| \equiv S(E, t) = S(E, t=0)$  are conserved. Using Eq. (7) with  $\boldsymbol{\Omega}_B(E) \equiv \Omega'_x E \hat{\mathbf{z}}$ , we find

$$\dot{\hat{\mathbf{S}}}(E, t) = \boldsymbol{\Omega}_B(E) \times \hat{\mathbf{S}}(E, t) + \sum_{E'} g(E, E') \mathbf{S}(E', t) \times \hat{\mathbf{S}}(E, t). \quad (8)$$

We solve Eq. (8) for the unit vectors  $\hat{\mathbf{S}}(E, t)$  in a quasiclassical approximation, treating  $\mathbf{S}(E, t)$  and  $\mathbf{S}(E', t)$  as classical vectors.

There is some flexibility in the definition of  $S(E)$ , as Eq. (8) is invariant under the scale transformation  $S(E) \rightarrow c(E) S(E)$  and  $g(E, E') \rightarrow g(E, E')/c(E)$ . We choose  $S(E, t=0)$  to be

$$S(E, t=0) = N_E/2. \quad (9)$$

Here  $N_E = N P(E)$  is the number of atoms in axial energy group  $E$ , with  $N$  the total atom number and  $P(E)$  the probability distribution. In the model, we take  $P(E)$  to be a zero-temperature Thomas-Fermi distribution for near-degenerate samples; for higher temperatures, we employ a Boltzmann distribution. The collective spin vectors begin their evolution after a  $\pi/2$  rf pulse coherently rotates the initially  $z$ -polarized sample, so that

$$\hat{\mathbf{S}}(E, t=0) = \hat{\mathbf{x}}', \quad (10)$$

where  $\hat{\mathbf{x}}'$  is defined in the Bloch frame, orthogonal to  $\hat{\mathbf{z}}$ .

For our choice of  $S(E, t=0)$  in Eq. (9), and the interaction potential of Eq. (4), the site-to-site couplings  $g(E, E')$  in Eq. (8) are given by

$$g(E, E') = -\bar{n}_\perp \frac{8\pi\hbar}{m} \int dx |\phi_E(x)|^2 |\phi_{E'}(x)|^2 a_S \quad (11)$$

where  $\phi_E(x)$  is the axial trap eigenstate for energy  $E$ . Note that spatiotemporal optical control of interactions [28] allows  $a_S \rightarrow a_S(x, t)$ , so that  $g(E, E')$  may be tailored to create designer quantum simulators.

In Eq. (11), we have assumed that the single-particle probability density takes the form  $\mathcal{R}(\rho) |\phi_E(x)|^2$ , where  $x$  is the axial coordinate,  $\rho$  is the transverse radial coordinate,  $\mathcal{R}(\rho)$  is the transverse probability density, and  $\int d\rho 2\pi\rho \mathcal{R}(\rho) = 1$ . The overlap integral is evaluated using a WKB approximation. For a harmonic trap,

$$\begin{aligned} \int dx |\phi_E(x)|^2 |\phi_{E'}(x)|^2 &= \frac{2}{\pi^2} \sqrt{\frac{m\bar{\omega}_x^2}{2|E-E'|}} \\ &\times \text{elliptic } K \left[ -\frac{\min(E, E')}{|E-E'|} \right]. \end{aligned} \quad (12)$$

The average transverse probability density is given by

$$\bar{n}_\perp \equiv \int d\rho 2\pi\rho \mathcal{R}^2(\rho). \quad (13)$$

For lossless evolution,  $\mathcal{R}(\rho)$  is time independent. Assuming a zero-temperature Thomas-Fermi distribution,

$$\mathcal{R}(\rho) = \frac{3}{\pi\sigma_\rho^2} \left( 1 - \frac{\rho^2}{\sigma_\rho^2} \right)^2, \quad (14)$$

we obtain  $\bar{n}_\perp = 9/(5\pi\sigma_\rho^2)$ . For the Maxwell-Boltzmann distribution,

$$\mathcal{R}(\rho) = \frac{1}{\pi\sigma_\rho^2} e^{-\rho^2/\sigma_\rho^2}, \quad (15)$$

$$(8) \quad \text{we find } \bar{n}_\perp = 1/(\pi\sigma_\rho^2).$$

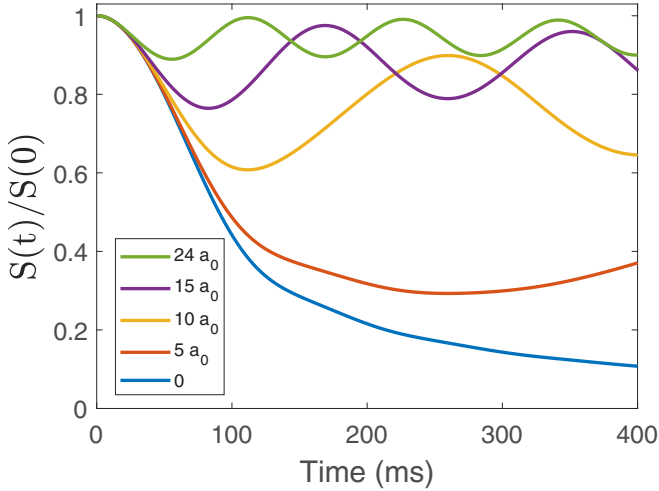


FIG. 3. Predicted magnitude of the total spin vector as a function of time for loss-free evolution with different  $s$ -wave scattering lengths. In the model, we use the experimental parameters given in the text. For  $a_s/a_0 = 0, 5, 10, 15, 24$  (bottom to top), the respective interaction strengths are  $\zeta = 0, 0.8, 1.6, 2.4, 3.9$ .

The evolution of the collective spin vectors is determined by the competition between  $\Omega_B(E) \equiv \Omega'_x E \hat{z}$  and  $\omega_{MF}(E, t) \equiv \sum_{E' \neq E} g(E, E') \mathbf{S}(E', t)$  in Eq. (8). As the lattice is not in thermal equilibrium, this competition results in two *dynamical* phases: a spin-unlocked phase, where the spread in  $\omega_B(E)$  dominates, and a spin-locked phase, where  $\omega_{MF}(E, t) \propto a_s$  dominates, independent of the sign of  $a_s$ . With increasing  $|a_s|$ , the lattice exhibits a crossover between these two dynamical phases [25, 27]. As the pseudospins are initially spin polarized, they cannot interact until  $\omega_B(E)$  causes the collective spin vectors to fan out with  $E$ -dependent angles in the transverse plane. We characterize the crossover by the dimensionless interaction strength [27],

$$\zeta \equiv \bar{g}/(\Omega'_x \sigma_E \sqrt{2}), \quad (16)$$

which is the ratio of the average mean-field frequency to the spread in the precession rates. For small  $a_s$ ,  $\zeta$  is small and  $\omega_B(E)$  dominates, which is reflected in a low magnitude of the total spin vector  $S(t) = |\sum_E \mathbf{S}(E, t)|$  (Fig. 3). We find that when  $a_s$  is large enough that  $\zeta \gtrsim 1.5$ ,  $\omega_{MF}(E, t)$  dominates over  $\omega_B(E)$  and the spins lock together. However, spin locking produces parallel spins that suppress the identical spin-rotation rate  $\propto \mathbf{S}(E) \times \mathbf{S}(E')$ , enabling  $\omega_B(E)$  to again fan out the spin vectors, which then reenables scattering and subsequent spin locking, resulting in an oscillation of  $S(t)$  (Fig. 3). With increasing  $\zeta \propto |a_s|$ , the average  $S(t)$  (magnetization) increases and the oscillation amplitude decreases.

### III. MODELING TWO-BODY LOSS IN THE ENERGY-SPACE SPIN LATTICE

Inelastic interactions are induced in the energy-space spin lattice by illuminating the coherently prepared clouds with an optical field (Fig. 1). In this section, we describe our model for the spin-dependent loss in this system due to these interactions.

We begin by describing the two-body collisional interaction (Fig. 1) in more detail. For the high magnetic fields of interest, a collision between a pair of  $^6\text{Li}$  atoms, one in each of the two lowest hyperfine spin states, occurs nominally in the triplet  $^3\Sigma_u$  electronic potential (where “triplet” refers to the two-electron spin state). For  $s$ -wave scattering, where the relative motion state is symmetric in the interchange of the two atoms, the *two-atom* hyperfine state is the antisymmetric spin state:

$$\begin{aligned} |\Psi_a(1, 2)\rangle &= \frac{1}{\sqrt{2}} (|\uparrow_z\rangle_1 |\downarrow_z\rangle_2 - |\downarrow_z\rangle_1 |\uparrow_z\rangle_2) \\ &\simeq |1, -1; 1, 1\rangle. \end{aligned} \quad (17)$$

Here, at the high magnetic fields used in the experiments,  $|1, -1; 1, 1\rangle$  is the dominant triplet spin state in the interior basis, i.e., the total electronic spin state is  $S = 1, M_S = -1$ , and the total nuclear spin state is  $I = 1, M_I = 1$ . This triplet state has a large hyperfine coupling to the dominant singlet  $S = 0$  electronic state [34], denoted  $|g_1\rangle$ , which is in the 38th vibrational state of the singlet  $^1\Sigma_g$  ground molecular potential, producing a broad Feshbach resonance at 832.2 G [35]. The difference between the magnetic moments of the singlet and triplet states enables magnetic tuning of the  $s$ -wave scattering length near the resonance. The applied optical field drives transitions from  $|g_1\rangle$  to the 64th vibrational state in the electronically excited singlet  $^1\Sigma_u$  molecular potential, denoted  $|e\rangle$  [8, 11]. Spontaneous emission from  $|e\rangle$  causes the interaction to be inelastic, and we assume that the emission results in loss of both atoms without transfer of atoms between energy states, so that the energy-space spin lattice model remains appropriate.

Loss due to two-body inelastic collisions between a particle of species  $A$  and a particle of species  $B$  is generally modeled as

$$\dot{n}_A(\mathbf{r}, t) = \dot{n}_B(\mathbf{r}, t) = -K_2^{AB} n_A(\mathbf{r}, t) n_B(\mathbf{r}, t) \quad (18)$$

where  $n_A(\mathbf{r}, t)$  is the three-dimensional (3D) density of species  $A$  and  $n_B(\mathbf{r}, t)$  is the 3D density of species  $B$ . It is assumed that only  $A$  and  $B$  interact, and that each inelastic collision causes both atoms to be lost. Equation (18) follows from the definition of the inelastic cross section of the  $AB$  interaction  $\sigma_{\text{inel}}^{AB}$  where  $K_2^{AB} \equiv \langle v_{\text{rel}} \sigma_{\text{inel}}^{AB} \rangle$  (the brackets denote the average over the relative speeds  $v_{\text{rel}}$ ). This will be the basis for constructing our loss model.

#### Optically induced loss in the energy lattice

To treat loss in the energy-space spin lattice, we consider the atoms at each energy site  $E$  to be a “species” in the context of Eq. (18). We associate a 3D density  $n_E(\mathbf{r}, t)$  to the group of atoms with energy  $E$  and a collective spin vector  $\mathbf{S}(E, t)$ , and sum the inelastic collision rates for atoms of energy with  $E$  with atoms of energies  $E'$  over all  $E' \neq E$  to obtain

$$\dot{n}_E(\mathbf{r}, t) = - \sum_{E'} K(E, E', t) n_{E'}(\mathbf{r}, t) n_E(\mathbf{r}, t). \quad (19)$$

Here the total density is  $n(\mathbf{r}, t) = \sum_E n_E(\mathbf{r}, t)$  and  $K(E, E', t)$  is the effective energy-dependent two-body loss rate coefficient.



We obtain  $K(E, E', t)$  by computing the probability that the pair of atoms in energy groups  $E$  and  $E'$  is in the anti-symmetric spin state  $|\Psi_a(1, 2)\rangle$  of Eq. (17). We assume that the spin of each atom of energy  $E$  is polarized along  $\hat{\mathbf{S}}(E, t)$ , corresponding to the spin state  $|\hat{\mathbf{S}}(E, t)\rangle$ . In this case, atoms of energies  $E$  and  $E'$  are in states with definite spin polarizations, so that we can assume the incoming spin state for a colliding pair of atoms with energies  $E$  and  $E'$  is  $|\hat{\mathbf{S}}(E, t)\rangle_1 |\hat{\mathbf{S}}(E', t)\rangle_2$ . The probability amplitude to be in the antisymmetric spin state is then the inner product of the incoming spin state with  $|\Psi_a(1, 2)\rangle$ , so that

$$K(E, E', t) = K_2^a |\langle \Psi_a(1, 2) | \hat{\mathbf{S}}(E, t)\rangle_1 |\hat{\mathbf{S}}(E', t)\rangle_2|^2 \quad (20)$$

where  $K_2^a$  is the loss constant associated with the antisymmetric two-atom spin state, given in Eq. (17). Suppressing the time dependence, the energy-dependent spin states take the form

$$\begin{aligned} |\hat{\mathbf{S}}(E)\rangle_1 &= e^{-i\frac{\phi_E}{2}} \cos\left(\frac{\theta_E}{2}\right) |\uparrow_z\rangle_1 + e^{i\frac{\phi_E}{2}} \sin\left(\frac{\theta_E}{2}\right) |\downarrow_z\rangle_1, \\ |\hat{\mathbf{S}}(E')\rangle_2 &= e^{-i\frac{\phi_{E'}}{2}} \cos\left(\frac{\theta_{E'}}{2}\right) |\uparrow_z\rangle_2 + e^{i\frac{\phi_{E'}}{2}} \sin\left(\frac{\theta_{E'}}{2}\right) |\downarrow_z\rangle_2. \end{aligned}$$

A straightforward calculation gives

$$\begin{aligned} |\langle \Psi_a(1, 2) | \hat{\mathbf{S}}(E, t)\rangle_1 |\hat{\mathbf{S}}(E', t)\rangle_2|^2 \\ = \frac{1}{4} [1 - \cos \theta_E \cos \theta_{E'} - \sin \theta_E \sin \theta_{E'} \cos(\phi_E - \phi_{E'})]. \end{aligned} \quad (21)$$

With this result, Eq. (20) can be written in terms of the unit vectors. Restoring the time dependence,

$$K(E, E', t) \equiv \frac{K_2^a}{4} [1 - \hat{\mathbf{S}}(E, t) \cdot \hat{\mathbf{S}}(E', t)], \quad (22)$$

which has an analogous structure to the projection operator of Eq. (1). As expected, when the collective spin vectors for energy groups  $E$  and  $E'$  are parallel, the corresponding unit vectors  $\hat{\mathbf{S}}(E, t)$  and  $\hat{\mathbf{S}}(E', t)$  are parallel and there is no loss. In contrast, maximum loss occurs when the unit vectors are antiparallel,  $K(E, E', t) \rightarrow K_2^a/2$ . The unit vectors  $\hat{\mathbf{S}}(E, t)$  are found from Eq. (8), with  $S(E, t) = N_E(t)/2$ , where the atom number  $N_E(t)$  is self-consistently determined from Eqs. (19) and (22), as we now show.

We assume that the spin-energy correlated 3D densities  $n_E(\mathbf{r}, t)$  can be factored as

$$n_E(\mathbf{r}, t) = n_E(x, \rho, t) = N_E(t) \mathcal{R}(\rho, t) |\phi_E(x)|^2, \quad (23)$$

where  $x$  is the axial coordinate and  $\rho$  is the transverse coordinate. As observed in the experiments and shown in Fig. 6 below, for nonzero  $K_2^a$ , the increase in the loss rate with increasing 3D density reshapes the spatial profile. For this reason, we assume that both the atom number  $N_E(t)$  in each energy group and the transverse probability density  $\mathcal{R}(\rho, t)$  are functions of time. Further, we assume that  $\mathcal{R}(\rho, t)$  is independent of  $E$ , and take  $\int d\rho 2\pi\rho \mathcal{R}(\rho, t) = 1$  for all  $t$ . Using Eq. (23), the spatial integral of the total density,  $n(\mathbf{r}, t) = \sum_E n_E(\mathbf{r}, t)$ , yields the total atom number:

$$N(t) = \sum_E N_E(t). \quad (24)$$

Using Eq. (23) in Eq. (19) and integrating over  $x$ , we obtain

$$\begin{aligned} \frac{d}{dt} [N_E(t) \mathcal{R}(\rho, t)] \\ = - \sum_{E'} \eta(E, E', t) [N_{E'}(t) \mathcal{R}(\rho, t)] [N_E(t) \mathcal{R}(\rho, t)], \end{aligned} \quad (25)$$

where

$$\eta(E, E', t) \equiv K(E, E', t) \int dx |\phi_E(x)|^2 |\phi_{E'}(x)|^2. \quad (26)$$

Integrating Eq. (25) over  $\rho$  and using Eq. (28), we find

$$\begin{aligned} \dot{N}_E(t) \int d\rho 2\pi\rho \mathcal{R}(\rho, t) + N_E(t) \frac{d}{dt} \int d\rho 2\pi\rho \mathcal{R}(\rho, t) \\ = -\bar{n}_\perp(t) \sum_{E'} \eta(E, E', t) N_{E'}(t) N_E(t), \end{aligned} \quad (27)$$

where  $\bar{n}_\perp(t)$  is the time-dependent average transverse probability density:

$$\bar{n}_\perp(t) \equiv \int d\rho 2\pi\rho \mathcal{R}^2(\rho, t). \quad (28)$$

Since  $\int d\rho 2\pi\rho \mathcal{R}(\rho, t) = 1$ , Eq. (27) immediately yields

$$\dot{N}_E(t) = -\bar{n}_\perp(t) \sum_{E'} \eta(E, E', t) N_{E'}(t) N_E(t). \quad (29)$$

Next, we sum Eq. (25) over  $E$  and use Eq. (24) to obtain

$$\begin{aligned} \dot{N}(t) \mathcal{R}(\rho, t) + N(t) \dot{\mathcal{R}}(\rho, t) \\ = -\mathcal{R}^2(\rho, t) \sum_E \sum_{E'} \eta(E, E', t) N_{E'}(t) N_E(t) \\ = \dot{N}(t) \frac{\mathcal{R}^2(\rho, t)}{\bar{n}_\perp(t)}. \end{aligned} \quad (30)$$

Here, the right-hand side has been simplified by using the sum of Eq. (29) over  $E$  and Eq. (24):

$$\dot{N}(t) = -\bar{n}_\perp(t) \sum_E \sum_{E'} \eta(E, E', t) N_{E'}(t) N_E(t). \quad (31)$$

Hence, the radial probability distribution obeys

$$\dot{\mathcal{R}}(\rho, t) = \frac{\dot{N}(t)}{N(t)} \left[ \frac{\mathcal{R}^2(\rho, t)}{\bar{n}_\perp(t)} - \mathcal{R}(\rho, t) \right]. \quad (32)$$

Using Eq. (28), one readily verifies that the integral of Eq. (32) over  $\rho$  vanishes, so that the total transverse probability remains normalized to 1 for all  $t$ . Further, the right-hand side is  $\propto \dot{N}(t) [\mathcal{R}(\rho, t) - \bar{n}_\perp(t)]$ , where  $\dot{N}(t) < 0$  when  $K_2^a \neq 0$ . Hence, near the center of the cloud, where  $\mathcal{R}(\rho, t) > \bar{n}_\perp(t)$ , the probability density decreases in time, while in the wings, where  $\mathcal{R}(\rho, t) < \bar{n}_\perp(t)$ , the probability density increases in time. The net effect of the loss is to increase the effective width of  $\mathcal{R}(\rho, t)$ , while preserving the normalization.

#### IV. EVOLUTION OF THE ENERGY-SPACE SPIN LATTICE WITH LOSS

To model the energy-space spin lattice with optically induced loss, we employ Eqs. (29) and (32), together with

Eq. (8). These equations determine the evolution of the density for each energy group, the transverse profile and therefore the total density and the total number in the presence of loss, which are compared with measurements.

Including the  $E$ -dependent loss, the magnitudes of the collective spin vectors in Eq. (8),  $S(E, t) = N_E(t)/2$ , decrease with time. As noted above [Eq. (6)], the evolution of  $\mathbf{S}(E, t)$  includes both a rotation of the unit vectors and a time-dependent magnitude:

$$\dot{\mathbf{S}}(E, t) = S(E, t) \dot{\hat{\mathbf{S}}}(E, t) + \dot{S}(E, t) \hat{\mathbf{S}}(E, t). \quad (33)$$

The unit vectors  $\hat{\mathbf{S}}(E, t)$  evolve according to Eq. (8), while the decay of the magnitudes  $S(E, t)$  is determined by Eq. (29) with  $N_E(t) = 2S(E, t)$  and Eqs. (26) and (22):

$$\begin{aligned} \dot{S}(E, t) = & - \sum_{E'} \kappa(E, E', t) [S(E, t)S(E', t) \\ & - \mathbf{S}(E, t) \cdot \mathbf{S}(E', t)]. \end{aligned} \quad (34)$$

Here, the effective loss rate  $\kappa(E, E', t)$  is given by

$$\kappa(E, E', t) \equiv \frac{K_2^a}{2} \bar{n}_\perp(t) \int dx |\phi_E(x)|^2 |\phi_{E'}(x)|^2. \quad (35)$$

We discuss the determination of  $K_2^a$  for mixtures in Secs. IV and VB.

We rewrite the evolution of the transverse probability density [Eq. (32)] as

$$\dot{\mathcal{R}}(\rho, t) = \frac{\dot{S}(t)}{S(t)} \left[ \frac{\mathcal{R}^2(\rho, t)}{\bar{n}_\perp(t)} - \mathcal{R}(\rho, t) \right]. \quad (36)$$

Here we have defined  $S(t) \equiv \sum_E S(E, t) = N(t)/2$ . Equation (28) shows that the site-to-site couplings of Eq. (11) become time dependent for  $K_2^a \neq 0$ ,  $g(E, E') \rightarrow g(E, E', t)$ , while the decay of  $S(E, t)$  reduces the rotation rate of the unit vectors by reducing the magnitude of the mean field.

Including loss, the evolution of the energy-dependent collective spin vectors is determined by Eq. (33), using Eq. (8) to describe the rotation of the unit vectors and Eqs. (28), (34), and (36) to determine the decay of the magnitudes. The collective spin vectors are initialized according to Eqs. (9) and (10). The initial condition for the transverse probability density,  $\mathcal{R}(\rho, 0)$ , is given by Eq. (14) for a Thomas-Fermi distribution and by Eq. (15) for a Maxwell-Boltzmann distribution.

### Optically induced loss in a mixture

For the loss model described above, we require the loss constant  $K_2^a$  associated with a pair of atoms in the antisymmetric two-atom spin state  $|\Psi_a(1, 2)\rangle$ . To obtain  $K_2^a$ , we measure the loss in a 50 : 50 incoherent mixture of  $|\uparrow_z\rangle$  and  $|\downarrow_z\rangle$ , for which the 50 : 50 ratio is maintained throughout the evolution, and extract the fraction of the loss constant associated with the state  $|\Psi_a(1, 2)\rangle$ . Considering the mixture to be composed of atoms in the  $|\uparrow_z\rangle$  state and the  $|\downarrow_z\rangle$  state, we define the 3D densities associated with each state  $n_\uparrow(\mathbf{r}, t)$  and  $n_\downarrow(\mathbf{r}, t)$  and apply Eq. (18) to obtain

$$\dot{n}_\uparrow(\mathbf{r}, t) = \dot{n}_\downarrow(\mathbf{r}, t) = -K_2^{\uparrow\downarrow} n_\uparrow(\mathbf{r}, t) n_\downarrow(\mathbf{r}, t). \quad (37)$$

We assume that the incoming state is a product state  $|\uparrow_z\rangle_1 |\downarrow_z\rangle_2$ . Then, the probability to be in the antisymmetric

two-atom spin state is  $|\langle \Psi_a(1, 2) | \uparrow_z \rangle_1 | \downarrow_z \rangle_2|^2 = 1/2$ :

$$K_2^{\uparrow\downarrow} = K_2^a \times 1/2. \quad (38)$$

With  $n_\uparrow(\mathbf{r}, t) + n_\downarrow(\mathbf{r}, t) = n(\mathbf{r}, t)$  the total density and  $n_\uparrow(\mathbf{r}, t) = n_\downarrow(\mathbf{r}, t) = n(\mathbf{r}, t)/2$  for a 50 : 50 mixture, Eq. (37) yields

$$\dot{n}(\mathbf{r}, t) = -\frac{1}{4} K_2^a n^2(\mathbf{r}, t). \quad (39)$$

The analytic solution to Eq. (39) is readily obtained:

$$n(\mathbf{r}, t) = \frac{n(\mathbf{r}, 0)}{1 + \frac{1}{4} K_2^a n(\mathbf{r}, 0) t}. \quad (40)$$

Integrating Eq. (40) over all three spatial dimensions, the total atom number  $N(t)$  is predicted as a function of time, given  $n(\mathbf{r}, 0)$ :

$$N(t) = \int dx \int 2\pi \rho d\rho \frac{n(\mathbf{r}, 0)}{1 + \frac{1}{4} K_2^a n(\mathbf{r}, 0) t}. \quad (41)$$

To measure  $K_2^a$ , then, we fit measurements of the atom number  $N(t)$  in the 50 : 50 mixture to Eq. (41). This is further described in Sec. VB, where we show that  $K_2^a$  is independent of the relative speed near the zero crossing of the broad Feshbach resonance in  $^6\text{Li}$  [see Eq. (46)]. However, as will also be discussed in Sec. VB, we must halve the measured  $K_2^a$  before inserting it into Eq. (21) in order to reach agreement with the loss measurements in the energy lattice.

## V. EXPERIMENTS

### A. Loss in energy-space spin lattices

To test the loss model, we measure the time-dependent decay of the total atom number  $N(t)$  in a cigar-shaped optical trap comprising a single focused  $\text{CO}_2$  laser beam. The measurements are obtained for scattering lengths  $a_s = 0$  to  $24 a_0$  at nominally the same density. Starting from a  $\hat{\mathbf{z}}$ -polarized sample, we employ a 0.5-ms  $\pi/2$  rf pulse to prepare an initially  $\hat{\mathbf{x}}$ -polarized sample. Immediately following the rf pulse, the trapped gas is illuminated by a uniform optical field locked on resonance with the singlet molecular  $|g_1\rangle \rightarrow |e\rangle$  transition (Fig. 1) and evolves for a variable amount of time  $0 \leq t \leq 400$  ms before absorption imaging of the atom densities for the  $|\uparrow_z\rangle$  and  $|\downarrow_z\rangle$  states, which are spectrally resolved.

In the experiments, we begin by evaporatively cooling a 50 : 50 mixture of atoms in the two lowest hyperfine states  $|\uparrow_z\rangle \equiv |1\rangle$  and  $|\downarrow_z\rangle \equiv |2\rangle$  at the broad Feshbach resonance near 832.2 G [35]. Following forced evaporation by lowering the trap depth, the trap depth is increased so that the radial trap frequency is  $\omega_\rho = 2\pi \times 668.0$  Hz. To avoid the formation of Feshbach molecules while tuning to the weakly interacting region near 527 G, the magnetic field is swept up to 1200 G and resonant light is applied to expel one spin state, leaving a  $\hat{\mathbf{z}}$ -polarized spin sample. The magnetic field is then swept to produce scattering length  $a_s(B)$  of interest near 527 G. The calibration of Ref. [24] determines  $a_s(B)$ , where magnetic field is measured by rf spectroscopy.

After this preparation, the total number of atoms  $N(0) \simeq 6.0 \times 10^4$ . A fit of the measured axial profile with a zero-temperature Thomas-Fermi distribution yields an axial width

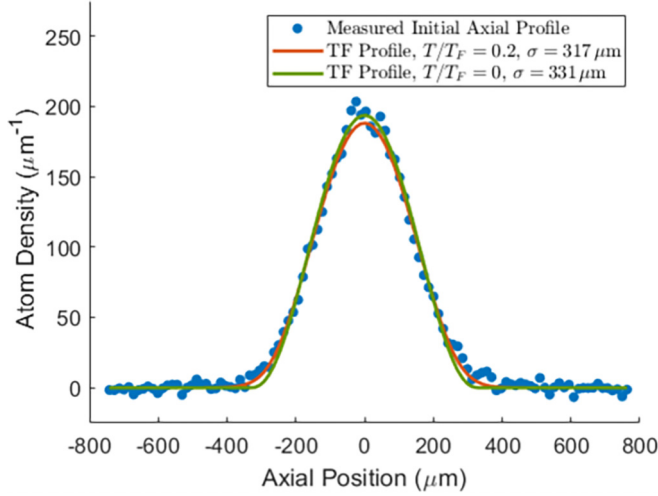


FIG. 4. Thomas-Fermi fits to the sum of the initial axial profiles of the  $|\uparrow_z\rangle$  and  $|\downarrow_z\rangle$  states, immediately after the  $\pi/2$  pulse, as used for measurement of  $N(t)$  at 0 bohr in the coherently prepared sample. The fit of a finite-temperature 1D Thomas-Fermi profile yields the reduced temperature  $T/T_F = 0.2$ . The fit is nearly identical to that of a zero-temperature 1D Thomas Fermi profile, justifying our use of a zero-temperature distribution in the model.

$\sigma_{\text{TF}}^x \simeq 331 \mu\text{m}$  (Fig. 4). The radial width  $\sigma_{\text{TF}}^\rho$  is computed from the ratio of trap transverse and axial frequencies,  $\omega_\rho \sigma_{\text{TF}}^\rho = \omega_x \sigma_{\text{TF}}^x$ . As noted in Sec. II, the curvature in the applied magnetic field results in a spin-dependent axial trapping force in the axial direction, where  $\omega_{\text{mag}} = 2\pi \times 16.3 \text{ Hz}$ . For the combined optical and magnetic trapping potentials near 527 G, the net axial trap frequency is measured to be  $\omega_x = 2\pi \times 25.0 \text{ Hz}$ . With  $\omega_\rho = 2\pi \times 668.0 \text{ Hz}$ , we find  $\sigma_{\text{TF}}^\rho \simeq 12.0 \mu\text{m}$ . To determine the temperature, we fit a 1D finite-temperature Thomas-Fermi distribution to the initial axial profile. The Fermi temperature  $T_F$  for our harmonic trap is determined by

$$E_F = k_B T_F = \hbar (6N\omega_\rho^2\omega_x)^{1/3}. \quad (42)$$

Note that the number 6 in Eq. (42) reflects the fact that all  $N$  atoms initially begin in an identical spin state. For the initial atom number and trap frequencies given in the last paragraph, we find  $T_F \simeq 0.75 \mu\text{K}$ . Using the calculated Thomas-Fermi radius  $\sigma_{\text{TF}}^x = \sqrt{2E_F/(m\omega_x^2)} \simeq 317.0 \mu\text{m}$ , a fit to a finite-temperature Thomas-Fermi profiles yields  $T \simeq 0.18 T_F$ . Figure 4 shows the averaged initial axial profile for a sample that is coherently prepared at 0 bohr, along with the corresponding fitted finite-temperature 1D Thomas-Fermi and zero-temperature 1D Thomas-Fermi profiles. The zero-temperature and finite-temperature Thomas-Fermi profiles are nearly identical, as expected for  $T \simeq 0.20 T_F$ , justifying the use of an effective zero-temperature profile with a fitted width in the model.

For every scattering length,  $K_2^a$  is measured from the loss in a 50 : 50 mixture, as discussed in Sec. VB. In all of the experiments, loss is induced by an optical beam propagating at an angle of  $\simeq 49^\circ$  relative to the trap  $x$  axis. The intensity half width at  $1/e$  of the optical beam is  $w = 1.1 \text{ mm}$ , so that the projection of the full width of the optical beam at  $1/e$  onto the cloud  $x$  axis is  $2w \sin(49^\circ) \simeq 1.5w = 1.6 \text{ mm}$ . This can

TABLE I. Two-body loss coefficients for 50 : 50 mixtures.

$a_S (a_0)$	$K_2^a (\mu\text{m}^3/\text{s})$	$\sigma_{K_2^a} (\mu\text{m}^3/\text{s})$
0	115	5
5	120	11.6
10	110	6.8
15	138	10
24	136	10

be compared to the full width of the cloud  $2\sigma_x \simeq 0.66 \text{ mm}$ . Hence, most of the atoms are illuminated near the peak intensity,  $I = P/(\pi w^2)$ . The servo-stabilized beam power is 7.6 mW, so that  $I = 2.0 \text{ mW/mm}^2$ . The Rabi frequency for the singlet electronic transition from the ground 38th vibrational state  $|g\rangle$  to the excited 64th vibrational state has been measured [28] to be  $\Omega_1/2\pi = 4.4 \text{ MHz} \sqrt{I[\text{mW/mm}^2]}$ . The Rabi frequency for the loss inducing beam is then  $\Omega_1 = 0.53 \times \gamma_e$ , where  $\gamma_e = 2\pi \times 11.8 \text{ MHz}$  is the rate of spontaneous emission from the excited molecular state [8,11]. The resonance frequency for each magnetic-field value is found by finding the peak loss in the incoherent mixture as a function of frequency, which is prepared as described in Sec. VB. Since the optical field is locked on resonance, there is no optical shift in the scattering length.

Measurements of the fraction of atoms remaining throughout the evolution  $N(t)/N(0)$  for coherently prepared samples are shown in Fig. 5, for several scattering lengths  $a_S$  and corresponding interaction strengths  $\zeta$  [Eq. (16)], along with the corresponding predictions using no free parameters. Predictions and measurements for  $a_S = 0 a_0$  ( $\zeta = 0$ ), where interactions are absent, are shown as a reference, and agree very well. The atom number is nearly stagnant for the first  $\approx 80 \text{ ms}$ , corresponding to the time needed for the energy-dependent Zeeman precession rates to separate the collective spin vectors. Once the spin vectors are sufficiently separated, the effective loss rate coefficient  $K(E, E', t)$  becomes non-negligible and the atom number begins to decay. At  $a_S = 5 a_0$  ( $\zeta = 1.03$ ), the data are almost indistinguishable from the  $a_S = 0 a_0$  case [Fig. 5(a)]. This is consistent with Fig. 3, where, for  $a_S = 5 a_0$  at our experimental densities, the system is still in the energy-dependent precession-dominated regime. The data show that a transition out of this dynamical phase occurs between  $a_S = 5 a_0$  and  $10 a_0$  ( $\zeta = 2.32$ ), where the measurements at  $a_S = 10 a_0$  exhibit the onset of loss suppression [Fig. 5(b)]. The loss is further suppressed for the  $a_S = 15 a_0$  ( $\zeta = 3.59$ ) data [Fig. 5(c)], and even more for the  $a_S = 24 a_0$  ( $\zeta = 5.39$ ) data [Fig. 5(d)], reflecting the increasing collective alignment of the spins, as shown for the lossless case of Fig. 3.

The importance of including the time dependence of  $\mathcal{R}(\rho, t)$  in the model can be seen in the difference between the predictions for  $\bar{n}_\perp = \bar{n}_\perp(0)$  and  $\bar{n}_\perp(t)$  at  $a_S = 0 a_0$ , as shown in Fig. 6. If  $\bar{n}_\perp$  is taken to be constant, the model disagrees with the data for longer times. Accounting for the decrease in  $\bar{n}_\perp(t)$  reduces the energy-dependent loss rate  $\kappa(E, E', t)$  of Eq. (35), causing the tail of the loss curve to rise to match the data.

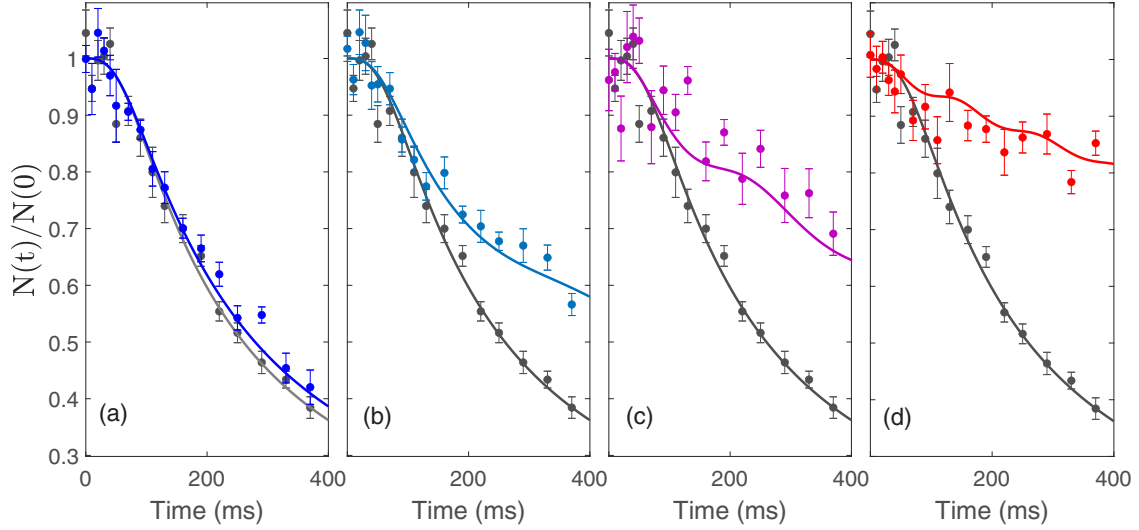


FIG. 5. Suppression of optically induced loss in a coherently prepared sample vs illumination time, for increasing scattering lengths.  $N(t)/N(0)$  is the atom fraction remaining after a time  $t$ . For reference, the lower black curves show the data and the model for a noninteracting gas  $a_S = 0 a_0$  ( $\zeta = 0$ ). Each point represents the average of six shots, and the error bar is the standard deviation of the mean. (a)  $a_S = 5 a_0$  ( $\zeta = 1.03$ ). (b)  $a_S = 10 a_0$  ( $\zeta = 2.32$ ). (c)  $a_S = 15 a_0$  ( $\zeta = 3.59$ ). (d)  $a_S = 24 a_0$  ( $\zeta = 5.39$ ). For each scattering length, the predicted curve employs *half* the value of  $K_2^a$  measured for the same scattering length in a 50 : 50 mixture (Table I). Note that the interaction strength  $\zeta$  [Eq. (16)] is not precisely linear in the scattering length due to slight variations in the density.

### B. Two-body loss constant $K_2^a$ in a mixture

To measure the two-body loss constant  $K_2^a$ , we measure the decay of the total number of atoms in an incoherent mixture of the  $|\uparrow_z\rangle$  and  $|\downarrow_z\rangle$  states. We employ a 50 : 50 mixture for which Eq. (39) is valid, and use Eq. (41) to fit the data,

allowing  $K_2^a$  to be determined from measurements of  $N(t)$ . We model  $n(\mathbf{r}, 0)$  as the Maxwell-Boltzmann distribution, which is appropriate for the higher-temperature samples used in the mixture measurements:

$$n(\mathbf{r}, 0) = \frac{N(0)}{\pi \sigma_\rho^2 \sigma_x \sqrt{\pi}} e^{-(\rho/\sigma_\rho)^2 - (x/\sigma_x)^2}, \quad (43)$$

where the axial size  $\sigma_x$  is determined from the measured spatial profiles. The radial size  $\sigma_\rho$  is then found from the ratio of the trap frequencies. Using the initial density  $n(\mathbf{r}, 0)$  in Eq. (41), the measured decay of the total number  $N(t)$  determines  $K_2^a$ , which is used as a fit parameter. Here we expect that  $K_2^a$  is independent of temperature, as discussed below [see Eq. (46)].

To prepare the sample, a 50 : 50 incoherent mixture of atoms in spin states  $|\uparrow_z\rangle$  and  $|\downarrow_z\rangle$  undergoes forced evaporation at 300 G. The magnetic field is then swept upward to the magnetic field of interest in the weakly interacting regime. This method avoids the formation of Feshbach molecules and subsequent loss. However, the efficiency of evaporation performed at 300 G, where the elastic scattering cross section is small, is reduced compared to that of the unitary gas at 832.2 G. For this reason, the samples used to measure  $K_2^a$  are at a higher temperature than for the coherently prepared samples. We assume that  $K_2^a$  is temperature independent, as  $K_2^a$  is expected to exhibit a weak momentum dependence in the weakly interacting regime. At the magnetic field of interest, the loss-inducing optical field is applied, and the total number of atoms is measured as a function of time. The optical resonance frequency is determined by finding the peak loss point at each magnetic field of interest. Using the measured initial axial width and the initial radial width deduced from the ratio of the trap frequencies, the initial density profile is determined

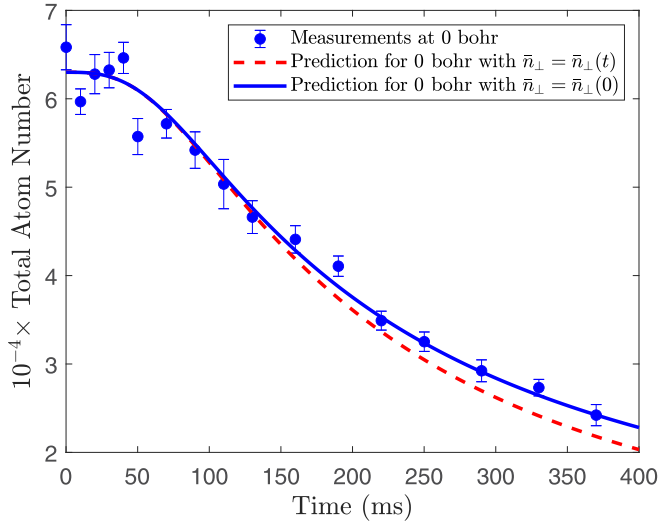


FIG. 6. Predictions of loss in a coherently prepared sample, with (blue solid) and without (red dashed) the time dependence of the average transverse probability density  $\bar{n}_\perp$ . The time dependence of  $\bar{n}_\perp(t)$  arises from loss. Measurements for 0 bohr in the coherently prepared cloud are in agreement with the model when  $\bar{n}_\perp = \bar{n}_\perp(t)$  (blue solid). When  $\bar{n}_\perp$  is taken to be constant (red dashed), the tail of the loss curve does not agree with the measurements. For the 0-bohr data, the inputs into the loss model are  $K_2^a = 58.0 \mu\text{m}^3/\text{s}$ , the initial atom number  $N = 6.3 \times 10^4$ , and the width  $\sigma_{\text{TF}} = 331.0 \mu\text{m}$ .



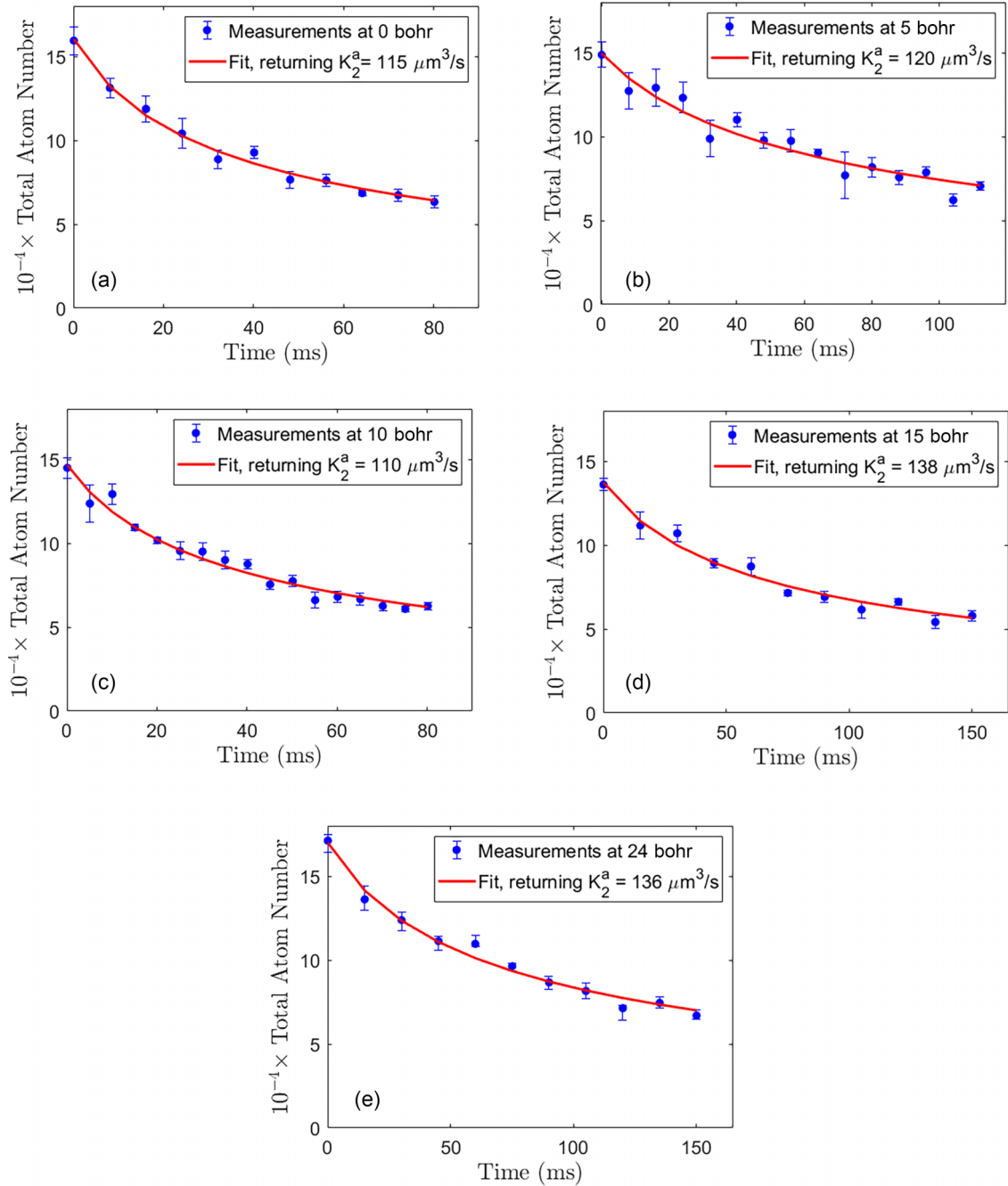


FIG. 7. Measurements and predictions of loss in the 50 : 50 mixture at each scattering length. Different trap depths were used for 0 and 10 bohrs ( $\omega_\rho = 2\pi \times 1075$  Hz,  $\omega_x = 2\pi \times 34$  Hz) than for 5, 15, and 24 bohrs ( $\omega_\rho = 2\pi \times 675$  Hz,  $\omega_x = 2\pi \times 23$  Hz). (a) Loss at 0 bohr, with an initial Gaussian width 213  $\mu\text{m}$ . (b) Loss at 5 bohrs, with an initial Gaussian width 241  $\mu\text{m}$ . (c) Loss at 10 bohrs, with an initial Gaussian width 211  $\mu\text{m}$ . (d) Loss at 15 bohrs, with an initial Gaussian width 243  $\mu\text{m}$ . (e) Loss at 24 bohrs, with an initial Gaussian width 260  $\mu\text{m}$ .

and Eq. (39) is used to find  $K_2^a$ . This procedure is repeated for each scattering length  $a_S$  employed in the experiments.

We determine the temperature from a fit of a Maxwell-Boltzmann distribution to the spatial profiles,  $k_B T = m\omega_x^2 \sigma_x^2 / 2$ , where  $\sigma_x$  is the fitted Gaussian width. For 15  $a_0$ , this procedure gives  $T = 0.56 T_F$ , where  $T_F = 0.79 \mu\text{K}$  is determined by

$$T_F = \frac{\hbar}{k_B} (3N\omega_\rho^2 \omega_x)^{1/3}. \quad (44)$$

Note that we have used a factor 3 = 6/2 in place of the factor 6 in Eq. (42), as a 50 : 50 mixture has half of the total number of atoms  $N$  in each spin state.

Measurements of  $N(t)$  in 50 : 50 mixtures are shown in Fig. 7 for all of the scattering lengths of interest, using Eq. (41) to determine  $K_2^a$ . The values extracted from the fit are displayed in Table I, where the uncertainty  $\sigma_{K_2^a}$  is determined from the square root of the covariance matrix of the fit (note that this neglects the uncertainty in the initial density). The measured value of  $K_2^a$  changes by  $\simeq 10\%$  as

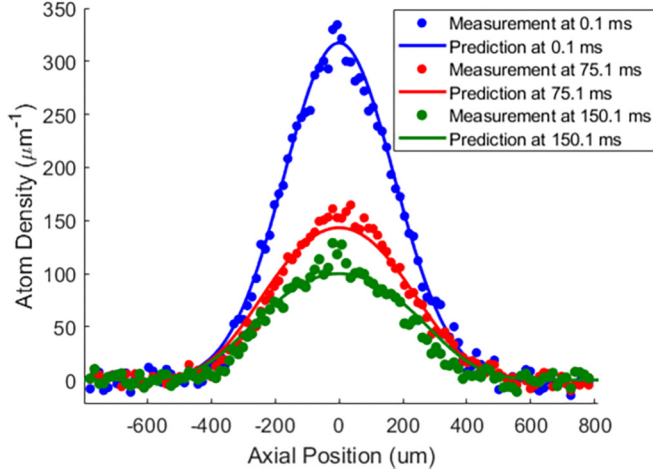


FIG. 8. Measurements and predictions of Eq. (45) for the evolution of the axial profiles in a mixture at 0.1 ms (top), 75.1 ms (middle), and 150.1 ms (bottom). The magnetic field is tuned so that  $a_s = 15 a_0$ . The two-body loss rate constant  $K_2^a = 2 \times 69.0 \mu\text{m}^3/\text{s}$  is determined from the fit of  $N(t)$  [Eq. (41)] to the data.

the scattering length is varied, most likely due to changes in the optical detuning and alignment from run to run. Note that the axial widths are smaller for the measurements at 0 and 10  $a_0$  than for 5, 15, and 24  $a_0$ . The difference arises from the difference between the trap depths used for 0 and 10  $a_0$ , where the trap frequencies were  $\omega_\rho = 2\pi \times 1075$  Hz and  $\omega_x = 2\pi \times 34$  Hz. The 5, 15, and 24  $a_0$  data employed the smaller trap frequencies given in Sec. V A. The faster timescales of loss for the 0 and 10  $a_0$  measurements reflect the higher density of the sample in the deeper trap.

Equation (40) also predicts the time-dependent axial profiles  $n_{1D}(x, t)$ , which can be compared to measurements. For the Maxwell-Boltzmann distribution of Eq. (43),

$$n_{1D}(x, t) = \int d\rho \, 2\pi \rho \, n(\mathbf{r}, \mathbf{t}) = \frac{4\pi\sigma_\rho^2}{K_2^a t} \ln \left[ 1 + \frac{K_2^a t}{4\pi\sigma_\rho^2} \frac{N(0)}{\sigma_x \sqrt{\pi}} e^{-(x/\sigma_x)^2} \right]. \quad (45)$$

In the limit  $K_2^a t \rightarrow 0$ ,  $n_{1D}(x, t)$  approaches a 1D Gaussian distribution normalized to the initial total atom number  $N(0)$ , as it should. Using the  $K_2^a$  determined from the fit to  $N(t)$ , we find that the predicted axial profiles are in quantitative agreement with the measured profiles, as shown for  $a_s = 15 a_0$  in Fig. 8.

Initially, we used the measurements in Table I to determine the energy-dependent loss rate coefficient  $\kappa(E, E', t)$  of Eq. (35). However, we found that the loss model does not agree with the measurements in the energy lattice. To obtain quantitative agreement between predictions and data for coherently prepared samples, shown in Fig. 5 above, we need to divide the values of  $K_2^a$  measured in the mixture by a factor of 2. It is possible that we have incorrectly extracted  $K_2^a$  by using Eqs. (39) and (41).

### C. Predicting the two-body loss constant $K_2^a$

To gather evidence as to whether or not the factor of 1/2 is correct, we can compare the values of  $K_2^a$  used in the fits for the coherently prepared samples in Fig. 5 to predictions for the optically induced loss rate constant in  $^6\text{Li}$ . We take  $K_2^{\text{calc}} = -2 \times \frac{8\pi\hbar}{m} a''$ , where  $a'' < 0$  is determined from the complex light-induced phase shift  $\phi$  using  $\tan \phi = -ik a''$  at the optical resonance. Here,  $\hbar k$  is the relative momentum, and we assume  $|k a''| \ll 1$  as is the case for our experiments. Note that a factor of 2 is included to be consistent with the antisymmetrized hyperfine state of Eq. (17) that defines  $K_2^a$ , which in turn requires a symmetrized spatial state with a total cross section [36]  $\sigma_{\text{tot}} = 8\pi/k \text{Im}\{f(0)\}$  and an elastic cross section  $\sigma_{\text{el}} = 8\pi |f|^2$ , with  $f$  the  $s$ -wave scattering amplitude. The corresponding inelastic cross section  $\sigma_{\text{inel}} = \sigma_{\text{tot}} - \sigma_{\text{el}} = 2 \times \frac{\pi}{k^2} (1 - |e^{2i\phi}|^2)$  is twice that of Ref. [11], where the scattering atoms were treated as distinguishable and a factor  $4\pi$  was used in the cross sections, which is equivalent to Eq. (38) above. The Supplemental Material of Ref. [11] determines  $a''$  using  $x = k|a_{bg}|$  and  $\tilde{\Delta}_0 = (B - B_\infty)/\Delta B = -1$  in Eq. (S5) [37], which gives  $L(\tilde{\Delta}_0, x) \simeq 1$  in Eq. (S8), yielding

$$K_2^{\text{calc}} = 2 \times \frac{8\pi\hbar |a_{bg}|}{m} \frac{\hbar \gamma_e}{4\mu_B \Delta B} \tilde{\Omega}_1^2, \quad (46)$$

where  $\tilde{\Omega}_1 \equiv \Omega_1/\gamma_e$ . With the parameters of Ref. [38],  $a_{bg} = -1405 a_0$ ,  $\Delta B = 300$  G,  $\mu_B/\hbar = 2\pi \times 1.4$  MHz/G, and  $\gamma_e = 2\pi \times 11.8$  MHz, we find  $K_2^{\text{calc}} = 277.4 \mu\text{m}^3/\text{s} \tilde{\Omega}_1^2$ . This gives  $K_2^{\text{calc}} = 69.4 \mu\text{m}^3/\text{s}$  at  $\tilde{\Omega}_1 = 0.5$ , as used in the measurements. This result is in good agreement with the value  $K_2^a = 69 \mu\text{m}^3/\text{s}$  that fits the decay of the coherently prepared sample at 15  $a_0$ , but is, however, half the value  $K_2^a = 138 \mu\text{m}^3/\text{s}$  extracted from measurements at 15  $a_0$  in the 50 : 50 mixture using Eq. (39), as noted above.

## VI. CONCLUSIONS

We have the observed and explained dynamical collective suppression of optically induced inelastic scattering in a coherently prepared, weakly interacting Fermi gas. As the scattering length is increased at fixed initial density, we observe a crossover from high to low loss. We understand this suppression via the Pauli principle, where the system undergoes a crossover into a magnetized dynamical phase with parallel collective spin vectors, causing suppression of  $s$ -wave scattering and loss.

Our loss model quantitatively agrees with observations and incorporates the many-body evolution of the collective spin vectors. We find that the average of the values of the two-body loss constant  $K_2^a$  used to generate the curves for coherently prepared samples in Fig. 5,  $62 \pm 6.2 \mu\text{m}^3/\text{s}$ , is in good agreement with the predicted value of  $69.4 \mu\text{m}^3/\text{s}$ . This work paves the way for tailoring of spin-spin couplings by optical control of spin-spin interactions in energy-space lattices, as the accompanying loss can now be included in the models and is mitigated in magnetized states.

We also extract  $K_2^a$  from loss measurements in a 50 : 50 mixture. For these measurements, we assume that a pair of colliding atoms is in the product state  $|1\rangle_i |2\rangle_j$  and hence has a probability  $|\langle \Psi_a(i, j) | 1\rangle_i |2\rangle_j|^2 = 1/2$  to be in the

antisymmetric spin state. However, with this assumption, we find that the values of  $K_2^a$  used in the model to fit the data for coherently prepared samples need to be *half* of those extracted from measurements in a 50 : 50 mixture. At present, we are unable to resolve this discrepancy, which may arise from applying Eq. (39) to a very weakly interacting mixture or from an incorrect choice of the incoming two-atom state in deriving Eq. (39). Future studies of imbalanced spin mixtures and

imbalanced superposition states in weakly interacting Fermi gases may help to elucidate this problem.

### ACKNOWLEDGMENTS

Primary support for this research is provided by AFOSR Grant No. FA9550-22-1-0329. Additional support is provided by NSF Grants No. PHY-2006234 and No. PHY-2307107.

- 
- [1] G. B. Partridge, K. E. Strecker, R. I. Kamar, M. W. Jack, and R. G. Hulet, Molecular probe of pairing in the BEC-BCS crossover, *Phys. Rev. Lett.* **95**, 020404 (2005).
  - [2] M. Junker, D. Dries, C. Welford, J. Hitchcock, Y. P. Chen, and R. G. Hulet, Photoassociation of a Bose-Einstein condensate near a Feshbach resonance, *Phys. Rev. Lett.* **101**, 060406 (2008).
  - [3] S. Lapp, J. Ang'ong'a, F. A. An, and B. Gadway, Engineering tunable local loss in a synthetic lattice of momentum states, *New J. Phys.* **21**, 045006 (2019).
  - [4] L. Zhou, H. Li, W. Yi, and X. Cui, Engineering non-Hermitian skin effect with band topology in ultracold gases, *Commun. Phys.* **5**, 252 (2022).
  - [5] J. Li, A. K. Harter, J. Liu, L. de Melo, Y. N. Joglekar, and L. Luo, Observation of parity-time symmetry breaking transitions in a dissipative Floquet system of ultracold atoms, *Nat. Commun.* **10**, 855 (2019).
  - [6] Z. Ren, D. Liu, E. Zhao, C. He, K. K. Pak, J. Li, and G.-B. Jo, Chiral control of quantum states in non-Hermitian spin-orbit-coupled fermions, *Nat. Phys.* **18**, 385 (2022).
  - [7] D. Bauer, M. Lettner, C. Vo, G. Rempe, and S. Dür, Control of a magnetic Feshbach resonance with laser light, *Nat. Phys.* **5**, 339 (2009).
  - [8] H. Wu and J. E. Thomas, Optical control of Feshbach resonances in Fermi gases using molecular dark states, *Phys. Rev. Lett.* **108**, 010401 (2012).
  - [9] T. L. Nicholson, S. Blatt, B. J. Bloom, J. R. Williams, J. W. Thomsen, J. Ye, and P. S. Julienne, Optical Feshbach resonances: Field-dressed theory and comparison with experiments, *Phys. Rev. A* **92**, 022709 (2015).
  - [10] L. W. Clark, L.-C. Ha, C.-Y. Xu, and C. Chin, Quantum dynamics with spatiotemporal control of interactions in a stable Bose-Einstein condensate, *Phys. Rev. Lett.* **115**, 155301 (2015).
  - [11] A. Jagannathan, N. Arunkumar, J. A. Joseph, and J. E. Thomas, Optical control of magnetic Feshbach resonances by closed-channel electromagnetically induced transparency, *Phys. Rev. Lett.* **116**, 075301 (2016).
  - [12] C. A. Royse, J. Huang, and J. E. Thomas, companion paper, Collective dynamical Fermi suppression of optically induced inelastic scattering, *Phys. Rev. Lett.* **133**, 083404 (2024).
  - [13] Y. Margalit, Y.-K. Lu, F. Çağr Top, and W. Ketterle, Pauli blocking of light scattering in degenerate fermions, *Science* **374**, 976 (2021).
  - [14] C. Sanner, L. Sonderhouse, R. B. Hutson, L. Yan, W. R. Milner, and J. Ye, Pauli blocking of atom-light scattering, *Science* **374**, 979 (2021).
  - [15] A. B. Deb and N. Kjærgaard, Observation of Pauli blocking in light scattering from quantum degenerate fermions, *Science* **374**, 972 (2021).
  - [16] R. Jannin, Y. van der Werf, K. Steinebach, H. L. Bethlem, and K. S. E. Eikema, Pauli blocking of stimulated emission in a degenerate Fermi gas, *Nat. Commun.* **13**, 6479 (2022).
  - [17] X. Du, L. Luo, B. Clancy, and J. E. Thomas, Observation of anomalous spin segregation in a trapped Fermi gas, *Phys. Rev. Lett.* **101**, 150401 (2008).
  - [18] X. Du, Y. Zhang, J. Petricka, and J. E. Thomas, Controlling spin current in a trapped Fermi gas, *Phys. Rev. Lett.* **103**, 010401 (2009).
  - [19] U. Ebling, A. Eckardt, and M. Lewenstein, Spin segregation via dynamically induced long-range interactions in a system of ultracold fermions, *Phys. Rev. A* **84**, 063607 (2011).
  - [20] F. Piéchon, J. N. Fuchs, and F. Laloë, Cumulative identical spin rotation effects in collisionless trapped atomic gases, *Phys. Rev. Lett.* **102**, 215301 (2009).
  - [21] S. S. Natu and E. J. Mueller, Anomalous spin segregation in a weakly interacting two-component Fermi gas, *Phys. Rev. A* **79**, 051601(R) (2009).
  - [22] C. Deutsch, F. Ramirez-Martinez, C. Lacroûte, F. Reinhard, T. Schneider, J. N. Fuchs, F. Piéchon, F. Laloë, J. Reichel, and P. Rosenbusch, Spin self-rephasing and very long coherence times in a trapped atomic ensemble, *Phys. Rev. Lett.* **105**, 020401 (2010).
  - [23] A. P. Koller, M. L. Wall, J. Munding, and A. M. Rey, Dynamics of interacting fermions in spin-dependent potentials, *Phys. Rev. Lett.* **117**, 195302 (2016).
  - [24] S. Pegahan, J. Kangara, I. Arakelyan, and J. E. Thomas, Spin-energy correlation in degenerate weakly interacting Fermi gases, *Phys. Rev. A* **99**, 063620 (2019).
  - [25] S. Smale, P. He, B. A. Olsen, K. G. Jackson, H. Sharum, S. Trotzky, J. Marino, A. M. Rey, and J. H. Thywissen, Observation of a transition between dynamical phases in a quantum degenerate Fermi gas, *Sci. Adv.* **5**, eaax1568 (2019).
  - [26] M. L. Wall, Simulating fermions in spin-dependent potentials with spin models on an energy lattice, *Phys. Rev. A* **102**, 023329 (2020).
  - [27] J. Huang and J. E. Thomas, Energy-resolved spin correlation measurements: Decoding transverse spin dynamics in weakly interacting Fermi gases, *Phys. Rev. A* **109**, L041301 (2024).
  - [28] N. Arunkumar, A. Jagannathan, and J. E. Thomas, Designer spatial control of interactions in ultracold gases, *Phys. Rev. Lett.* **122**, 040405 (2019).
  - [29] K. Hazzard and B. Gadway, Synthetic dimensions, *Phys. Today* **76**(4), 62 (2023).

- [30] C. Lhuillier and F. Laloë, Transport properties in a spin polarized gas, I, *J. Phys. (Paris)* **43**, 197 (1982).
- [31] E. P. Bashkin, Spin waves and quantum collective phenomena in Boltzmann gases, *Sov. Phys. Usp.* **29**, 238 (1986).
- [32] In Ref. [24], we show that  $\Delta_x = \delta\omega_x n(E)$ , where  $n(E) = E/(\hbar\omega_x)$  with  $\delta\omega_x = -\delta\mu/(2\mu_B)\omega_{\text{mag}}^2/\omega_x$  the difference between the harmonic oscillator frequencies for the upper and lower hyperfine states and  $\omega_{\text{mag}}$  the oscillation frequency atoms in the  $x$ -magnetic potential.
- [33] J. Huang, C. A. Royse, I. Arakelyan, and J. E. Thomas, Verifying a quasiclassical spin model of perturbed quantum rewinding in a Fermi gas, *Phys. Rev. A* **108**, L041304 (2023).
- [34] H. Wu and J. E. Thomas, Optical control of the scattering length and effective range for magnetically tunable Feshbach resonances in ultracold gases, *Phys. Rev. A* **86**, 063625 (2012).
- [35] G. Zürn, T. Lompe, A. N. Wenz, S. Jochim, P. S. Julienne, and J. M. Hutson, Precise characterization of  $^6\text{Li}$  Feshbach resonances using trap-sideband-resolved rf spectroscopy of weakly bound molecules, *Phys. Rev. Lett.* **110**, 135301 (2013).
- [36] E. Bratten and H.-W. Hammer, Universality in few-body systems with large scattering length, *Phys. Rep.* **428**, 259 (2006).
- [37] The  $(\tilde{\Delta}_0 - \epsilon x^2)$  in the denominator of Eq. (S5) in the Supplemental Material of Ref. [11] should be  $(\tilde{\Delta}_0 - \epsilon x^2)^2$ .
- [38] M. Bartenstein, A. Altmeyer, S. Riedl, R. Geursen, S. Jochim, C. Chin, J. H. Denschlag, R. Grimm, A. Simoni, E. Tiesinga, C. J. Williams, and P. S. Julienne, Precise determination of  $^6\text{Li}$  cold collision parameters by radio-frequency spectroscopy on weakly bound molecules, *Phys. Rev. Lett.* **94**, 103201 (2005).